Western Boundary Sea Level: A Theory, Rule of Thumb, and Application to Climate Models

SHOSHIRO MINOBE

Earth and Planetary Sciences, Faculty of Science, and Natural History Sciences, Graduate School of Science, Hokkaido University, Sapporo, Japan

MIO TERADA

Natural History Sciences, Graduate School of Science, Hokkaido University, Sapporo, Japan

BO QIU

Department of Oceanography, University of Hawai'i at Mānoa, Honolulu, Hawaii

NIKLAS SCHNEIDER

Department of Oceanography, and Hawaii International Pacific Research Center, University of Hawai'i at Mānoa, Honolulu, Hawaii

(Manuscript received 14 June 2016, in final form 23 February 2017)

ABSTRACT

To better understand coastal sea level variability and changes, a theory that predicts sea levels along a curved western boundary using interior ocean sea level information is proposed. The western boundary sea level at a particular latitude is expressed by the sum of contributions from interior sea levels propagating onto the western boundary by long Rossby waves between that latitude and a higher latitude, and from the western boundary sea level at the higher latitude. This theory is examined by using a linear, reduced gravity model. A comparison between the theory and the model shows good agreement. A simple scaling law (or rule of thumb) derived from the theory provides a measure of the higher-latitude sea level and ocean interior sea level contributions. The theory is then tested using data from 34 climate models in phase 5 of the Coupled Model Intercomparison Project (CMIP5) for dynamic sea level changes between the end of the twentieth and twenty-first centuries. The theory captures the nearly uniform sea level rise from the Labrador Sea to New York City (NYC), with a reduction in the increase of sea level farther south toward the equator, qualitatively consistent with the CMIP5 multimodel ensemble, even though the theory underestimates the equatorward reduction rate. Along the South American east coast, the theory successfully reproduced the spatial pattern of the sea level change. The theory suggests a strong link between a sea level rise hot spot along the northeastern coast of North America and the sea level increase in the Labrador Sea, consistent with the result that rates of NYC sea level rise are highly correlated to those in the Labrador Sea in CMIP5 models.

1. Introduction

Ocean dynamics plays important roles in sea level variability on interannual and decadal time scales (Di Lorenzo et al. 2008; Qiu and Chen 2012; Sasaki et al. 2008, 2013, 2014) and in spatial distribution of nonuniform sea level changes due to the global warming (e.g., Yin et al. 2010; Yin 2012; Suzuki and Ishii 2011a,b; Sueyoshi and Yasuda 2012; Zhang et al. 2014; Slangen et al. 2014). Sea level variability and changes have exerted a substantial socioeconomic impact via their coastal manifestations (Nicholls and Cazenave 2010; Carson et al. 2016). Yet, understanding of coastal sea levels, especially along the western boundary regions where strong western boundary currents exist, has advanced slowly in comparison with that of open ocean sea levels. For example, future sea level increases due to

Denotes content that is immediately available upon publication as open access.

Corresponding author e-mail: Shoshiro Minobe, minobe@sci.hokudai.ac.jp

DOI: 10.1175/JPO-D-16-0144.1

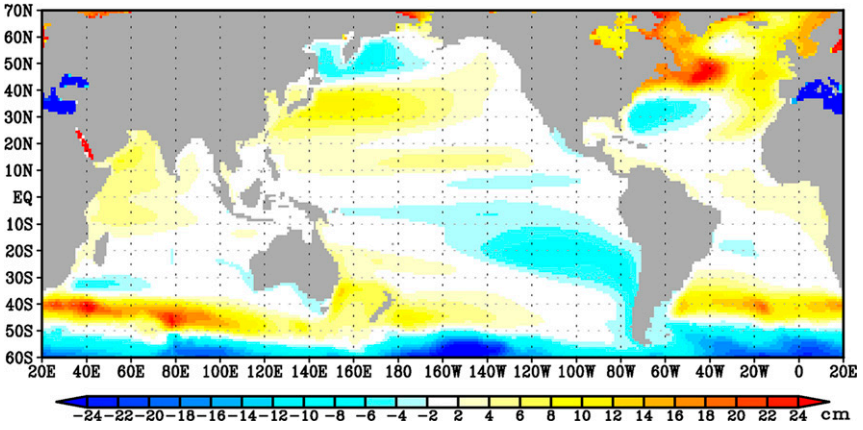

FIG. 1. Dynamical sea level change between the periods of 2081–2100 and 1981–2000 derived from MME under the RCP 8.5 scenario using 34 CMIP5 models. Data are plotted for grid points that are in the ocean in more than 80% of models after interpolation onto a common 1° × 1° grid.

ocean contributions are projected to be high in the northwestern Atlantic, southwestern South Atlantic, northwestern North Pacific, and southwestern South Pacific (Fig. 1; also see Yin et al. 2010; Church et al. 2013; Slangen et al. 2014). Interestingly, the offshore high sea level rise in the North Atlantic appears to impact sea level change at the northeastern coast of North America (which is known as a sea level rise hot spot) with a similar magnitude, but the amplitude of the strong sea level rise in the South Atlantic and North Pacific declines rapidly as it moves shoreward and does not reach the coast (e.g., Yin et al. 2010; Church et al. 2013; Carson et al. 2016).

At present, adequate explanations for the contrasting coastal and offshore sea level relations between the North Atlantic and the other basins are lacking, and this is largely due to the lack of our understanding of the western boundary sea level (WBSL) and its connection to offshore sea level changes. Previous studies have explained the mechanisms of sea level rises in the ocean interior. For example, the sea level rise in the North Atlantic is caused by the reduction of the Atlantic meridional overturning circulation and the weakening of North Atlantic deep convection (Yin et al. 2009, 2010; Yin and Goddard 2013), while the sea level rise pattern over the North Pacific is due to wind distribution changes (Yin et al. 2010; Sueyoshi and Yasuda 2012) or ocean heat uptake (Suzuki and Ishii 2011a).

Theoretical studies on the relationship between the western boundary and ocean interior variability can be divided into two groups. The first group investigated basinwide variability and obtained boundary solutions by requiring mass conservation in the basin. Earlier papers using this approach employed quasigeostrophic dynamics and assumed that the amplitude of boundary waves, including those along the western boundary, was uniform along all lateral boundaries (e.g., Milliff and McWilliams 1994; Liu et al. 1999). The assumption of uniform amplitude is appropriate for a meridionally narrow basin, but not for a wide one as emphasized by Johnson and Marshall (2002), who showed an equatorward reduction of sea level amplitude along the western boundary.

Recent papers that use reduced gravity, primitive equation models limit the assumption of uniform amplitude to the eastern boundary and provide WBSL solutions (Cessi and Louazel 2001; Zhai et al. 2014). Although these western boundary solutions are useful when working to understand how the WBSL responds to basin-scale forcing, they cannot be directly applied to sea level rise issues. Furthermore, these solutions are given for the meridional western boundary, but the actual western boundary can be slanted from a median.

The second group of studies investigated the relationship between the western boundary and the ocean interior more locally, rather than a part of the basin solution. In this context, the theory proposed by Godfrey (1975) is important. His theory, which is based on mass balance in the western boundary layer (WBL), indicates that the WBSL differences at two meridionally separated points normalized by their Coriolis parameters are proportional to the incident mass due to long Rossby waves traveling onto the western boundary. Godfrey's theory was used to examine meridional transport in the WBL by Kessler and Gourdeau (2007) and Durand et al. (2009).

The relationship between the WBSL and interior information was also studied by Pedlosky (1996), who showed that the WBSL is determined by an ocean-interior streamfunction in a steady, nondivergent system on a beta plane. Using Pedlosky's theory, Tsujino et al. (2008) built a semianalytical model for mean sea level around Japan and for transports at major straits around Japan.

We further extend these works, especially that of Godfrey (1975), with a focus on the relationship between WBSL and interior sea level. It should be emphasized that, to the authors' best knowledge, even though Kessler and Gourdeau (2007) and Durand et al. (2009) applied Godfrey's theory in realistic situations, no studies have validated the theory comprehensively using simple models such as the reduced gravity model. Godfrey (1975) examined his theory with a single-case numerical experiment and briefly reported that a rough calculation based on the theory underestimated modeled WBSL. Furthermore, Godfrey's theory was derived solely for a western boundary running meridionally, and no investigations have been conducted for more general meridionally slanted or curved western boundaries.

Since the expansion of the theory to these more realistic coastal geometries will clearly increase the value of the theory, the present paper has four objectives. The first is to expand Godfrey's theory to allow for a curved meridional western boundary, so that the relationship of the WBSL to interior sea levels can be more realistically evaluated. The second is to validate the theory using a simple numerical model. The third is to explore implications of the theory, which we will attempt through a scaling law (or rule of thumb). The fourth is to apply the theory to increasing sea levels along the western boundary, including the sea level rise hot spot on the northeastern North American coastline, using climate model outputs.

The rest of the paper is organized as follows. In section 2, a theory for the relationship between the WBSL and ocean interior sea level that allows for curved western boundary is derived. In section 3, a numerical model and an experiment design for validating the theory are described, and the results of a comparison between the theory and the model are shown in section 4. A rule of thumb derived from the theory and its implications are explained in section 5. In section 6, the theory is applied to the sea level rise along the western boundary in climate models. Conclusions and discussion are presented in section 7.

2. Theory

In this section, we derive a theory for the relationship between the WBSL and an interior sea level with a curved western boundary. We begin by considering a linearized reduced gravity model. The governing equations are

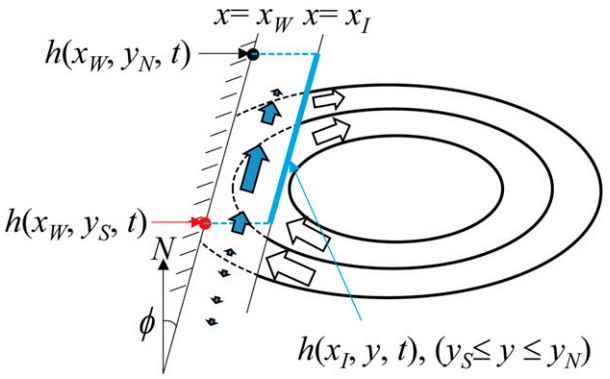

FIG. 2. Schematic of the situation considered in the present study. Contours indicate sea level due to a long Rossby wave incident to the western boundary layer. Contours are dashed in the western boundary layer because the full solution in this layer should be a superposition of the Rossby wave solution and western boundary solution. The open arrow indicates the geostrophic flow associated with the Rossby wave, which has positive sea level anomalies in this schematic, while the solid arrows indicate boundary layer flow. The mass input to the WBL due to the Rossby wave is transmitted equatorward by the boundary layer transport, resulting in southward transport to south of the latitude for positive sea level anomalies. The boundary layer transport is generally northward in interior sea level latitudes because of the geostrophy associated with positive interior sea level anomalies. The theory expresses the WBSL at the latitude y_S (red circle) with respect to WBSL at the higher latitude y_N (black circle) and the ocean sea level between two latitudes in the ocean interior (blue line). The angle between the western boundary and a meridian is shown by variable ϕ, which is measured from due north in the clockwise direction.

$$u_t - fv = -gh_x + A_v(u_{xx} + u_{yy}), \tag{1}$$

$$v_t + fu = -gh_y + A_v(v_{xx} + v_{yy}), \quad \text{and} \tag{2}$$

$$h_t(g/g') + H(u_x + v_y) = 0, \tag{3}$$

where x and y are the zonal and meridional coordinates, respectively; t is the time; h is the sea level; u and v are the zonal and meridional velocities, respectively; f is the Coriolis parameter; g is the gravitational acceleration; g' is the reduced gravity; H is the uniform upper layer thickness; and A_v is the horizontal viscosity coefficient. Linearized reduced gravity models are also used for recent theoretical studies of ocean responses to the wind and thermohaline forcings (e.g., Cessi and Louazel 2001; Zhai et al. 2014), which involves an assumption of $g' \ll g$ (e.g., section 3.2 of Vallis 2006) and $|h|g/g' \ll H$.

We will now consider the situation shown in the schematic of Fig. 2. In the ocean interior, sea level is governed by long Rossby waves that propagate westward, thereby yielding mass input to the WBL. The input mass is transmitted equatorward in the form of a Kelvin

wave or a Kelvin–Munk wave (Godfrey 1975), or in the form of a boundary wave associated with bottom friction (Marshall and Johnson 2013). It is not essential to our theory to determine which wave is actually involved, but it is important that equatorward propagation should occur regardless of the wave type. In this case, the WBSL at a particular latitude is given by the sum of contributions of the WBSL at the higher latitude and the interior sea level between two latitudes (Fig. 2), as derived below. Readers who are interested in the dynamics of Kelvin–Munk or boundary waves may refer to Godfrey (1975) and Marshall and Johnson (2013).

Next, we will consider mass conservation within the WBL, which spans between the western boundary at the zonal position of $x = x_W(y)$ and the western end of the ocean interior at $x = x_I(y)$ between the two latitudes of y_S and y_N (Fig. 2). We will limit our attention to a case where $x_W(y)$ is a single valued function. The area integral of continuity [Eq. (3)] using Gauss's theorem within the WBL under a non-normal flow boundary condition along the western boundary gives

$$\int_{y_S}^{y_N}\int_{x_W(y)}^{x_I(y)}\frac{g}{g'}h_t\,dx\,dy+\int_{l_S}^{l_N}Hu_n[x_I(y),y,t]\,dl+\int_{x_W(y_N)}^{x_I(y_N)}Hv(x,y_N,t)\,dx-\int_{x_W(y_S)}^{x_I(y_S)}Hv(x,y_S,t)\,dx=0, \tag{4}$$

where u_n is the perpendicular component of velocity with respect to $x_I(y)$, l is the coordinate along the western end of the ocean interior, and l_S and l_N are the positions corresponding to the northern and southern latitudes along l. The full solution (h, u, v) is assumed to be expressed by the superposition of the long Rossby wave solution (h_0, u_0, v_0) and the western boundary solution (h_b, u_b, v_b), that is, $(h, u, v) = (h_0, u_0, v_0) + (h_b, u_b, v_b)$. Note that this assumption restricts the theory to outside of the equatorial waveguide. Then, Eq. (4) is rewritten as

$$\int_{y_S}^{y_N}\int_{x_W(y)}^{x_I(y)}\frac{g}{g'}(h_0+h_b)_t\,dx\,dy+\int_{l_S}^{l_N}Hu_{0n}[x_I(y),y,t]\,dl+\int_{x_W(y_N)}^{x_I(y_N)}Hv(x,y_N,t)\,dx-\int_{x_W(y_S)}^{x_I(y_S)}Hv(x,y_S,t)\,dx=0, \tag{5}$$

where the perpendicular velocity contribution along $x_I(y)$ is expressed only by the Rossby wave solution u_0 because the boundary solution is absent in the ocean interior. As is widely known, long Rossby waves can be assumed to be in planetary geostrophic balance $(-fv_0 = -gh_{0x},\ fu_0 = -gh_{0y})$, which, combined with Eq. (3), indicates that the long Rossby waves satisfy

$$h_{0t}-h_{0x}g'H\beta/f^2=0, \tag{6}$$

where β is the meridional derivative of the Coriolis parameter. This equation means that sea level anomalies caused by the long Rossby wave of Eq. (6) propagate at its group velocity with the longwave limit, $C_R(y)$ ($C_R = g'H\beta/f^2$), which is fast (slow) in the lower (higher) latitudes. Substituting Eq. (6) into the first term of Eq. (5) and using the geostrophic relation for the second term of Eq. (5), we obtain

$$\int_{y_S}^{y_N}\int_{x_W(y)}^{x_I(y)}\frac{g}{g'}h_{bt}\,dx\,dy+\int_{y_S}^{y_N}\frac{gH\beta}{f^2}h_0[x_I(y),y,t]\,dy-\int_{y_S}^{y_N}\frac{gH\beta}{f^2}h_0[x_W(y),y,t]\,dy-\int_{l_S}^{l_N}H\frac{g}{f}\frac{\partial}{\partial l}h_0[x_I(y),y,t]\,dl+\int_{x_W(y_N)}^{x_I(y_N)}Hv(x,y_N,t)\,dx-\int_{x_W(y_S)}^{x_I(y_S)}Hv(x,y_S,t)\,dx=0. \tag{7}$$

Integration by parts of the fourth term of Eq. (7) using the relation

$$\frac{d}{dl}\frac{1}{f}=\frac{dy}{dl}\frac{d}{dy}\frac{1}{f}=-\frac{dy}{dl}\frac{\beta}{f^2} \tag{8}$$

gives

$$\int_{y_S}^{y_N}\int_{x_W(y)}^{x_I(y)}\frac{g}{g'}h_{bt}\,dx\,dy-\int_{y_S}^{y_N}\frac{gH\beta}{f^2}h_0[x_W(y),y,t]\,dy-\left\{\frac{Hg}{f}h_0[x_I(y),y,t]\right\}_{y_S}^{y_N}+\int_{x_W(y_N)}^{x_I(y_N)}Hv(x,y_N,t)\,dx-\int_{x_W(y_S)}^{x_I(y_S)}Hv(x,y_S,t)\,dx=0, \tag{9}$$

where the second term of Eq. (7) is canceled with a term obtained from the integration by parts.

The meridional velocity in the WBL can be approximated by geostrophic velocity, even for a nonmeridional western boundary, unless the angle between the western boundary and a meridian, ϕ in Fig. 2, is not extremely large, as will be shown in the appendix. Thus, the meridional velocities in Eq. (9) can be expressed by the total sea level difference between x_W and x_I. These total sea levels at x_I are canceled with the third term of Eq. (9), because $h = h_0$ in the ocean interior. Therefore, Eq. (9) becomes

$$\int_{y_S}^{y_N}\int_{x_W(y)}^{x_I(y)}\frac{g}{g'}h_{bt}\,dx\,dy-\int_{y_S}^{y_N}\frac{gH\beta}{f^2}h_0[x_W(y),y,t]\,dy-\frac{g}{f(y_N)}h[x_W(y_N),y_N,t]+\frac{g}{f(y_S)}h[x_W(y_S),y_S,t]=0. \tag{10}$$

To determine the relationship between the WBSL and sea level in the ocean interior, we need to evaluate the second term of Eq. (10) using the ocean interior sea level. The Rossby wave of Eq. (6) takes time lag $\delta(y)$ ($\delta = L_W/C_R$) to cross the WBL of width $L_W(y)$ ($L_W = x_I - x_W$), and thus $h_0[x_W(y), y, t] = h[x_I(y), y, t-\delta]$, with h_0 being h in the ocean interior. Furthermore, for time scales longer than the adjustment time of the western boundary sea level and currents, the time derivative in Eq. (10) is small, and thus negligible. Therefore, Eq. (10) can be written as

$$-\int_{y_S}^{y_N} \frac{gH\beta}{f^2} h[x_I(y), y, t-\delta(y)]\, dy - \frac{g}{f(y_N)} h[x_W(y_N), y_N, t] + \frac{g}{f(y_S)} h[x_W(y_S), y_S, t] = 0. \tag{11}$$

In the context of cause and effect for the WBSLs at two latitudes in the second and third terms of Eq. (11), it is appropriate to interpret the WBSL at the higher latitude as the cause and that at the lower latitude as the effect because of the abovementioned equatorward mass propagation caused by Kelvin or boundary waves along the western boundary. Therefore, Eq. (11) may be rewritten as

$$h[x_W(y), y, t] = \frac{f(y)}{f(y_P)} h[x_W(y_P), y_P, t] + f(y)\int_y^{y_P} \frac{\beta}{f^2} h[x_I(y'), y', t-\delta(y')]\, dy', \tag{12}$$

where y and y_P are the meridional positions of lower and higher latitudes, respectively, with the subscript P standing for "poleward," and are y_S (y_N) and y_N (y_S) in the previous equations in the Northern (Southern) Hemisphere. This equation means that the WBSL at the lower latitude is given by the sum of the WBSL at the higher latitude and the contribution of the incoming long Rossby wave between the two latitudes. In Eq. (12), the Coriolis parameter $f(y)$ appears in both the first and second terms on the right-hand side, which means that the WBSL reduces its amplitude equatorward for latitudes where incoming mass from the interior is absent, which is consistent with Johnson and Marshall (2002).

In some applications, one may be interested in meridional transport rather than sea level (Kessler and Gourdeau 2007; Durand et al. 2009). In this case, ignoring time derivative of boundary solution Eq. (9) can be modified as

$$\int_{x_W(y)}^{x_I(y)} v(x,y,t)\, dx = \int_{x_W(y_P)}^{x_I(y_P)} v(x,y_P,t)\, dx + \frac{g}{f(y)} h[x_I(y), y, t] - \frac{g}{f(y_P)} h[x_I(y_P), y_P, t] - \int_y^{y_N} \frac{g\beta}{f^2} h[x_I(y'), y', t-\delta(y')]\, dy'. \tag{13}$$

The time lag in Eqs. (12) or (13) can be ignored if the zonal scale of the phenomena is much larger than the boundary layer width, or if, equivalently, the time scale is much longer than the time delay of long Rossby waves crossing the WBL. In this case, Eq. (12) reduces to

$$h[x_W(y), y, t] = \frac{f(y)}{f(y_P)} h[x_W(y_P), y_P, t] + f(y)\int_y^{y_P} \frac{\beta}{f^2} h[x_I(y'), y', t]\, dy'. \tag{14}$$

This equation is appropriate for the interpretation of sea level rise and fall caused by the climate change expressed by epoch sea level differences because the time delay is much shorter than the epoch duration.

It is worth noting some of the interpretations derived from the above equation. The total derivative with respect to y along the western boundary of Eq. (14) divided by $f(y)$ gives

$$\frac{\partial}{\partial y}\left\{\frac{h[x_W(y), y, t]}{f(y)}\right\}\bigg|_{x_W} = -\frac{\beta}{f(y)^2} h[x_I(y), y, t]. \tag{15}$$

This equation indicates that the equatorward increase of WBSL normalized by the Coriolis parameter is proportional to incoming mass onto the WBL because of long Rossby waves. Also, evaluating the derivative of the denominator of Eq. (15) and multiplying f in both sides, we obtain

$$\frac{\partial h[x_W(y), y, t]}{\partial y}\bigg|_{x_W} = \frac{\beta}{f}\{h[x_W(y), y, t] - h[x_I(y), y, t]\}. \tag{16}$$

This equation means that as one moves lower latitudes, the WBSL tends to approach to the internal sea level with the e-folding scale of β/f.

Equations (12) and (14) have interesting implications. These equations mean that the WBSL is not dependent on friction, even though the existence of friction is important in the meridional momentum equation. Consistently, Zhai et al. (2014) noted that the WBSL is independent of the friction coefficient and the momentum balance detailed in the WBL. The equations further suggest that the WBSL in a model will be independent of how accurately the WBL is resolved. Even if the WBL is only coarsely represented, as long as the interior sea level is properly reproduced in the model, the WBSL can be accurately

obtained. These expected features are examined quantitatively using a numerical model in the next section.

3. Numerical model and experiment design

To examine the theory in the previous section, numerical model experiments were conducted. The numerical model is a linear, reduced gravity model on a sphere. The governing equations are essentially the same as Eqs. (1)–(3), but we add volume input Q as a forcing in the continuity equation [Eq. (3)] and horizontal diffusivity, that is,

$$h_t(g/g') + H(u_x + v_y) = (g/g')A_h(h_{xx} + h_{yy}) + Q, \qquad (17)$$

where A_h is the horizontal diffusivity coefficient. The reason why volume input is used as the forcing rather than wind stress is because it is easier to generate localized sea level anomalies in the ocean interior to facilitate understanding. The mass input is directly relevant for representing the effects of buoyancy forcing, which plays an important role in future sea level increases (Yin et al. 2009, 2010; Suzuki and Ishii 2011b; Johnson and Marshall 2002). In the context of wind forcing, the mass input can be interpreted as the wind stress curl. The reduced gravity is assumed to be $0.04\,\mathrm{m\,s^{-2}}$, the gravity acceleration is $9.8\,\mathrm{m\,s^{-2}}$, and the upper-layer thickness at rest is 200 m, leading to the gravity wave speed of $2.8\,\mathrm{m\,s^{-1}}$. The sea level h is proportional to the upper-layer thickness η, as $hg = \eta g'$. The model has a B grid, with the h point at the ocean–land boundary, so that the coastal sea level is a direct model output. This is a different configuration from the Bryan–Cox model (Bryan 1969), but the same as the Ocean General Circulation Model (OGCM) developed by the Meteorological Research Institute in Japan (e.g., Tsujino et al. 2008). The standard grid spacing is 0.5° in longitude and latitude, and the horizontal viscosity/diffusivity is $1000\,\mathrm{m^2\,s^{-1}}$ with the slip boundary condition.

The model domain used for the meridional boundary experiments comprises meridional and zonal walls with 100° longitudinal width and 70° latitudinal width from 10°S to 60°N. The eastern half of the domain and the 5° range from the northern boundary are sponge regions, where strong Rayleigh friction/Newtonian damping is applied, so that anomalies propagating toward the equator do not reenter the ocean interior as Rossby waves from the eastern boundary associated with the equatorial/coastal Kelvin waves. The experiments are either steady forcing experiments or initial value experiments. In the steady forcing experiments, localized mass input [Q in Eq. (17)] is specified as a monopole function given by

$$Q = \begin{cases} a\cos\left[\sqrt{\left(\dfrac{x-x_0}{L_x}\right)^2 + \left(\dfrac{y-y_0}{L_y}\right)^2}\,\dfrac{\pi}{2}\right] & \text{for} \quad \left(\dfrac{x-x_0}{L_x}\right)^2 + \left(\dfrac{y-y_0}{L_y}\right)^2 < 1, \\ 0 & \text{otherwise} \end{cases} \qquad (18)$$

where L_x and L_y are zonal and meridional half-widths of the forcing, respectively; x_0 and y_0 indicate the center of the forcing; and a is the amplitude, which is set as $1.0 \times 10^{-6}\,\mathrm{m\,s^{-1}}$. Equation (18) is also used to specify the initial value for the initial value experiments, with amplitude a being 1.0 m. The forcing half-widths are set as 10° in longitude and 5° in latitude, and the forcing center is at $x_0 =$ 30°E and y_0 is changed parametrically to take values 10°, 20°, 30°, and 40°N. The western boundary is at 0°E. Slanted western boundaries are also examined for the steady-state experiments with the forcing center at 20°N and 30°E and a boundary slope of ±25° and ±62° from due north within the 15°–25°N segment of the western boundary. The model is integrated until the responses reach steady state for the steady forcing experiments, for which only final states will be shown in the next section, or until the response becomes essentially zero for initial value experiments.

Since our theory in the previous section suggests that the WBSL is independent of the western boundary structure, this predicted feature is examined via a series of steady-state experiments with the grid spacing of 1.0° or 0.25°, or with one order of magnitude smaller viscosity ($100\,\mathrm{m^2\,s^{-1}}$), or with nonslip boundary condition, all forced by the mass input centered at 20°N and 30°E. These parameter differences can change the western boundary structures, but not the interior sea level, and the theory predicts that the WBSL should remain essentially the same.

To apply the theory to the numerical modeling results, it is necessary to specify the zonal distance from the western boundary to the ocean interior (aforementioned L_W). A visual inspection of a sea level field (not shown) indicates that, for meridional western boundary experiments, the appropriate distance is 3° in longitude or longer, but it should be 5° or longer for an experiment involving a sharply slanted western boundary. For simplicity, we choose the 5° zonal width for both the meridional and slanted boundary experiments.

4. Theory and numerical model comparison

Before we examine the WBSL closely, it may be useful to illustrate general features of interior sea level and flow fields for a few steady forcing experiments (Fig. 3). Sea

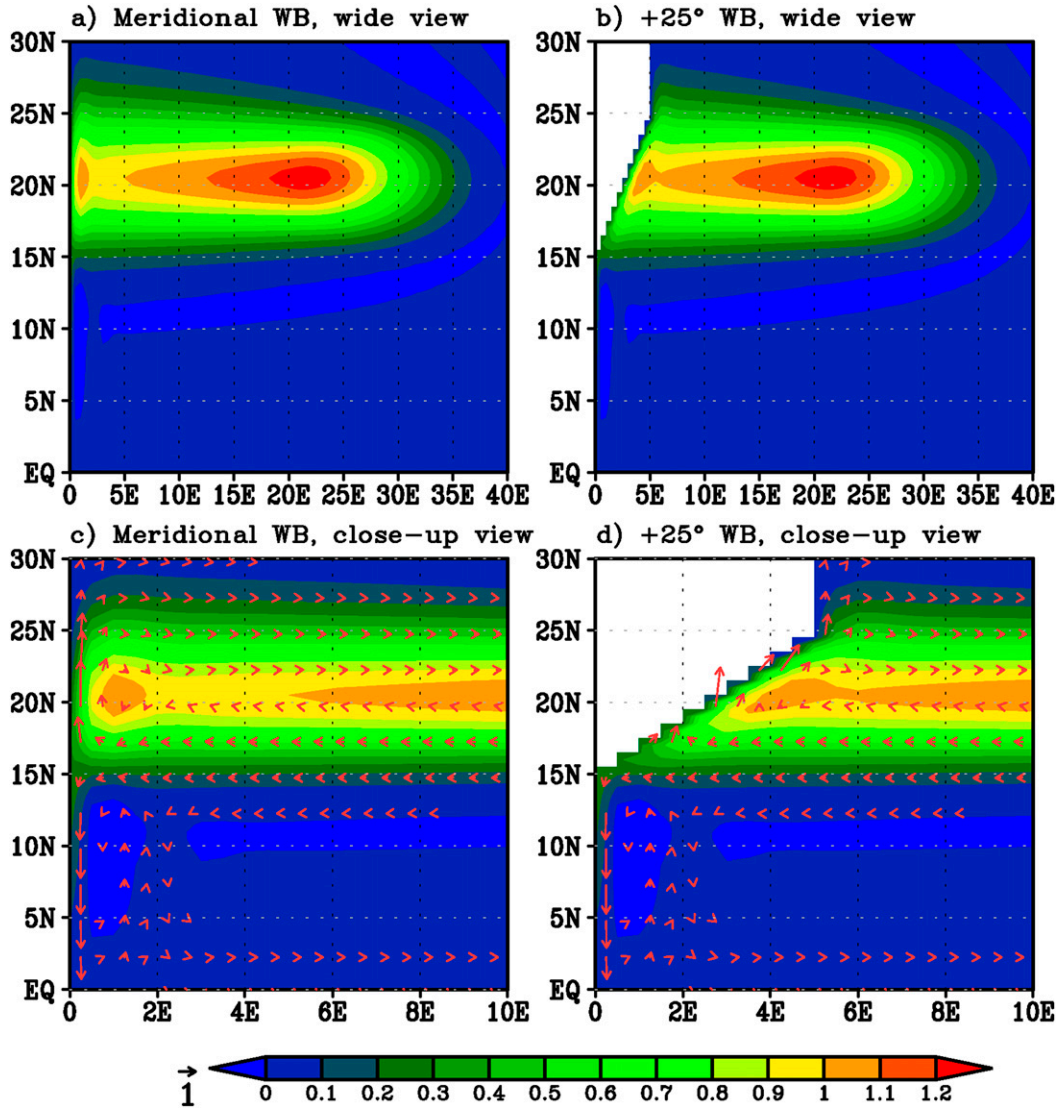

FIG. 3. Overview of sea level (color) and velocity (arrows in lower panels) responses in steady forcing experiments with (a),(c) the meridional boundary and (b),(d) the slanted boundary of a 25° angle from due north. The upper and lower panels show the same experiments, but the upper panels cover a wider longitudinal range extending from the western boundary to the mass-input forcing, centered at 20°N and 30°E, than the lower panels, which give close-up views of the western boundary layer. The amplitudes of each panel are normalized by the maximal sea level amplitude along 5°E in (a) (5.6 cm), and thus the sea level is unitless and the unit of velocity is 1 s^{-1}.

level anomalies propagate westward as long Rossby waves from the forcing region, with some widening due to horizontal diffusion. The meridional transport in the WBL to the incidental positive sea level is northward in the latitudes of the forcing, but is southward to the south, for both the meridional and slant western boundaries. This southward boundary flow is consistent with the fact that sea level anomalies reaching the western boundary must be ejected via Kelvin or boundary waves propagating equatorward (e.g., Godfrey 1975; Liu et al. 1999; Marshall and Johnson 2013).

For the steady forcing experiments, the theory is quite accurate for the WBSL, as shown in Fig. 4. The curves for the theoretically derived WBSL based on sea level at 5°E (western boundary is at 0°E) almost perfectly overlap the modeled WBSL for all of the four steady forcing experiments, regardless of the forcing latitude. The coastal sea level increases southward in the region where the westward propagating Rossby wave impacts the WBL, corresponding to the accumulation of mass to be transported equatorward, and then decreases southward monotonically according to the southward decrease of Coriolis

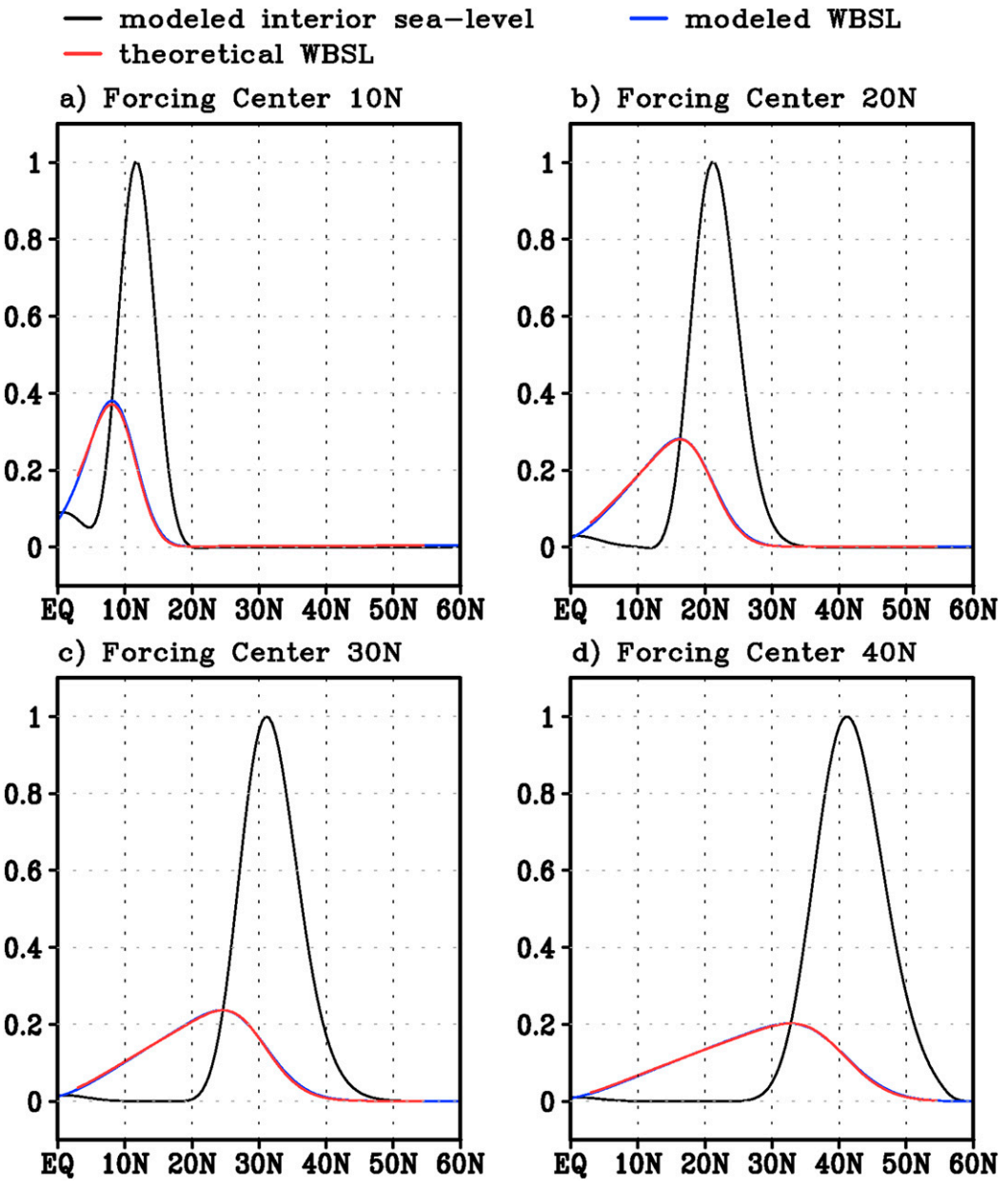

FIG. 4. Modeled sea level at the western end of ocean interior (5°E; black), the modeled WBSL (blue), and the theoretical WBSL (red) for steady forcing experiments with the meridional western boundary. The mass-input forcings are centered at 30°E and (a) 10°, (b) 20°, (c) 30°, and (d) 40°N. Sea levels are normalized by the maximal sea level along the western end of ocean interior in each panel [1.9, 5.6, 9.4, and 12.8 cm for (a)–(d), respectively].

parameter, as explained in the previous section (Fig. 4). Such localized WBSL responses cannot be found in a quasigeostrophic model, in which amplitude of the boundary solution is assumed to be uniform as explained in section 1. The aforementioned theory of Pedlosky (1996) predicts a southward increase of the WBSL in the latitudes of forcing, but constant amplitude to the south due to the beta-plane approximation.

The error of this theory is examined by calculating relative root-mean-square error (RRMSE), defined as

$$\mathrm{RRMSE} = \frac{\sqrt{\int_{y_1}^{y_2} \{h^M[x_W(y), y] - h^T[x_W(y), y]\}^2 dy}}{\sqrt{\int_{y_1}^{y_2} h^M[x_W(y), y]^2 dy}} \quad (19)$$

TABLE 1. RRMSE of the WBSL between the theory [Eq. (14)] and the numerical model for steady forcing experiments with the meridional western boundary.

Latitude of forcing center (°N)	10	20	30	40
RRMSE (%)	2.9	2.0	1.7	1.5

between 3°N and 55°N, where h^M is the modeled WBSL and h^T is the theoretical estimate of the WBSL using Eq. (14). RRMSEs are evaluated using the sea level at the eastern edge of the land. The RRMSE is less than 3% in all of the four steady forcing experiments with the meridional western boundary (Table 1), thereby confirming the validity of the theory.

As mentioned above, the theory implies that model parameters and setting do not influence the WBSL if the interior sea level is the same. This was examined by experiments with different grid spacing and viscosity from those of the standard setting and by a nonslip boundary condition experiment instead of a slip boundary condition. These parameter and boundary condition changes result in different sea level distributions inside of the WBL, especially around the latitudes of the forcing center (20°N) and south of the forcing latitudes (10°N; Figs. 5a,c). For example, one-tenth smaller viscosity coefficient reduces the Munk-layer thickness by half, which is consistent with the maximal sea level along 20°N closer to the western boundary than the standard case. However, the interior sea levels are essentially the same among the experiments (Fig. 5b), and the WBSLs are consistently almost identical (Fig. 5d). The RRMSEs for these experiments are generally smaller than 3%, except for the slightly higher value of 3.6% of the 1° grid spacing experiment. Therefore, the WBSL is not dependent on detailed WBL structures, as implied by the theory, which works well across different model parameters and boundary conditions.

Figure 6 shows maps of sea level with slanted western boundary for the steady forcing experiments with the forcing center at 20°N. The sea level distribution is essentially the same as that with the meridional boundary in the ocean interior, as shown by the collocation of sea level contours between the meridional boundary and the slanted boundary cases (Figs. 6b–e). The sea levels in the WBL, on the other hand, show differences between experiments. For example, the local sea level maximum in the WBL is prominent in the meridional boundary experiment (Fig. 6a), becomes weaker in the slanted boundary experiments of ±25° (Figs. 6b,c), and cannot be identified in the experiments of ±62° (Figs. 6d,e). Despite these differences, the theory provides a good approximation of the WBSL with an RRMSE less than 3% for the experiments with the boundary angle (ϕ in Fig. 2) of ±25° and less than 7% for those of ±62° (Table 2). Larger errors with a larger boundary angle are partly due to the effect of the horizontal diffusion because the RRMSEs in all these experiments become less than 3% when the horizontal diffusion coefficient is set to zero. The stronger diffusion effect for a more slanted western boundary is probably due to longer zonal distance over which long Rossby waves propagate in the slanted WBL. Nevertheless, the RRMSEs are small enough to allow us to conclude that the inclusion of the nonmeridional western boundary in our generalized theory is successful and valid.

An interesting feature in the experiments of slanted western boundary is that the sea level differences between the meridional and slanted western boundary experiments are smaller at the western boundary than at the western end of the ocean interior (Fig. 7). A more slanted western boundary in the current setting is associated with a more eastward location of the western boundary at the latitude of the forcing center. Consequently, sea levels at the eastern end of the WBL experience less diffusion in the strongly slanted boundary experiments and thus have larger and narrower peaks there than those in the meridional boundary experiment (Fig. 7a). The WBSL is, however, given by the integration of the interior sea levels [Eq. (14)], and therefore the flattening due to the diffusivity does not change the peak amplitude of the WBSL (Fig. 7b). This underlines the integral nature of the interior sea level influence on the WBSL.

For the time-dependent initial value experiments, the theory also provides good approximations for the numerical results. The WBSL follows interior sea level rising and falling with a southward shift (Fig. 8). This is well captured by the theory, thereby indicating that the WBSL is given by the meridional integration of incoming mass with an equatorward reduction associated with the Coriolis parameter. For RRMSEs of the initial value experiments, a time integral is also added in Eq. (19). The RRMSEs are generally larger than those in the steady forcing experiments, but still remain smaller than 10%, except for the slightly higher RRMSE (13%) for the initial anomaly imposed at 40°N (Table 3). The errors are mainly associated with the diffusion because, when the diffusion is set to zero, RRMSEs become less than about 3% for all experiments except for one with the initial value centered at 10°N. The beta-dispersion effect (Schopf et al. 1981) likely plays a role in Rossby wave propagation with this relatively low-latitude forcing and violates the assumption of the simple zonal propagation due to a long Rossby wave.

The longitudinal width of the WBL of 5° can be considered to be one order of magnitude smaller than the wavelength of the initial disturbance, given by twice the zonal extent of the monopole forcing width, that is, 40° wavelength. The time delay in Eq. (12) is, nevertheless, important. If we ignore the time delay, the theory predicts a faster peak

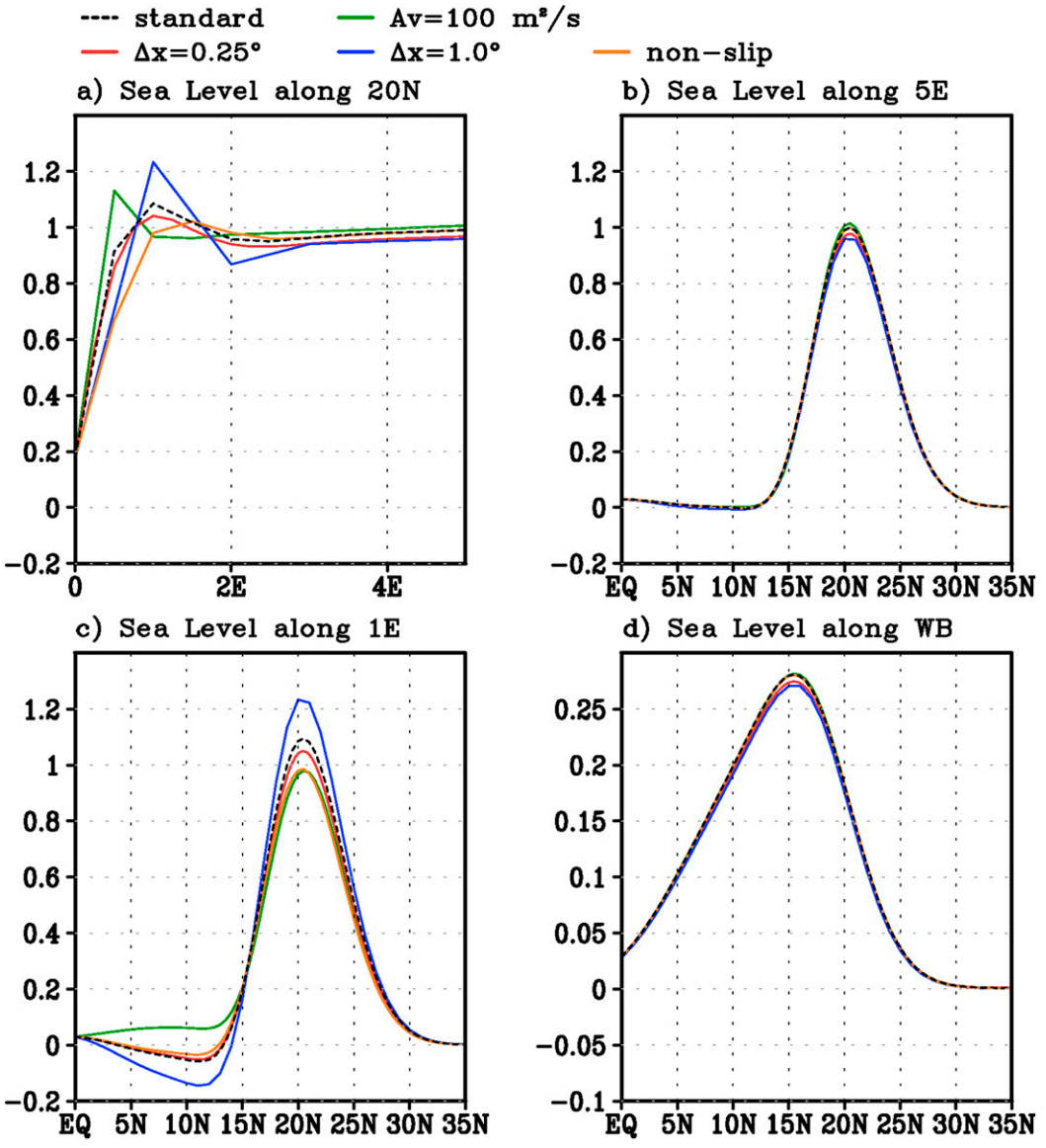

FIG. 5. Modeled sea level (a) along 20°N, (b) along the ocean interior western end (5°E), (c) in WBL (1°E), and (d) along the meridional western boundary (0°E) for steady forcing experiments with the different model parameters. Deviations from the standard parameter (sea level shown by black dashed curve) are small horizontal viscosity (100 $m^2 s^{-1}$; green) that is one-tenth of the standard value, halved grid spacing to 0.25° (red), doubled grid spacing to 1° (blue), and nonslip boundary condition (orange) instead of the standard slip boundary condition. The mass-input forcing is centered at 20°N and 30°E. Sea levels are normalized by the maximal sea level along the western end of ocean interior in the standard experiment (5.6 cm).

than shown in the model (Fig. 8), and the corresponding RRMSEs increase to about 30%–40% (Table 3). Consequently, our numerical experiments confirm that the theory, Eq. (12), works well for the time-dependent problems.

5. Rule of thumb

The successful reproduction of the WBSL by the theory shown in the previous section encouraged us to exploit implications of the theory relevant for the topic of sea level rise, for which the theory without the time delay [Eq. (14)] is appropriate, as mentioned above. It is important to note that Eq. (14) does not have any parameters relating to vertical structures (g' or H), and thus the equation holds for either a reduced gravity model or barotropic one-layer model, or any baroclinic vertical mode. Therefore, if superposition of vertical modes for sea level is appropriate within the WBL and each vertical mode obeys the linear

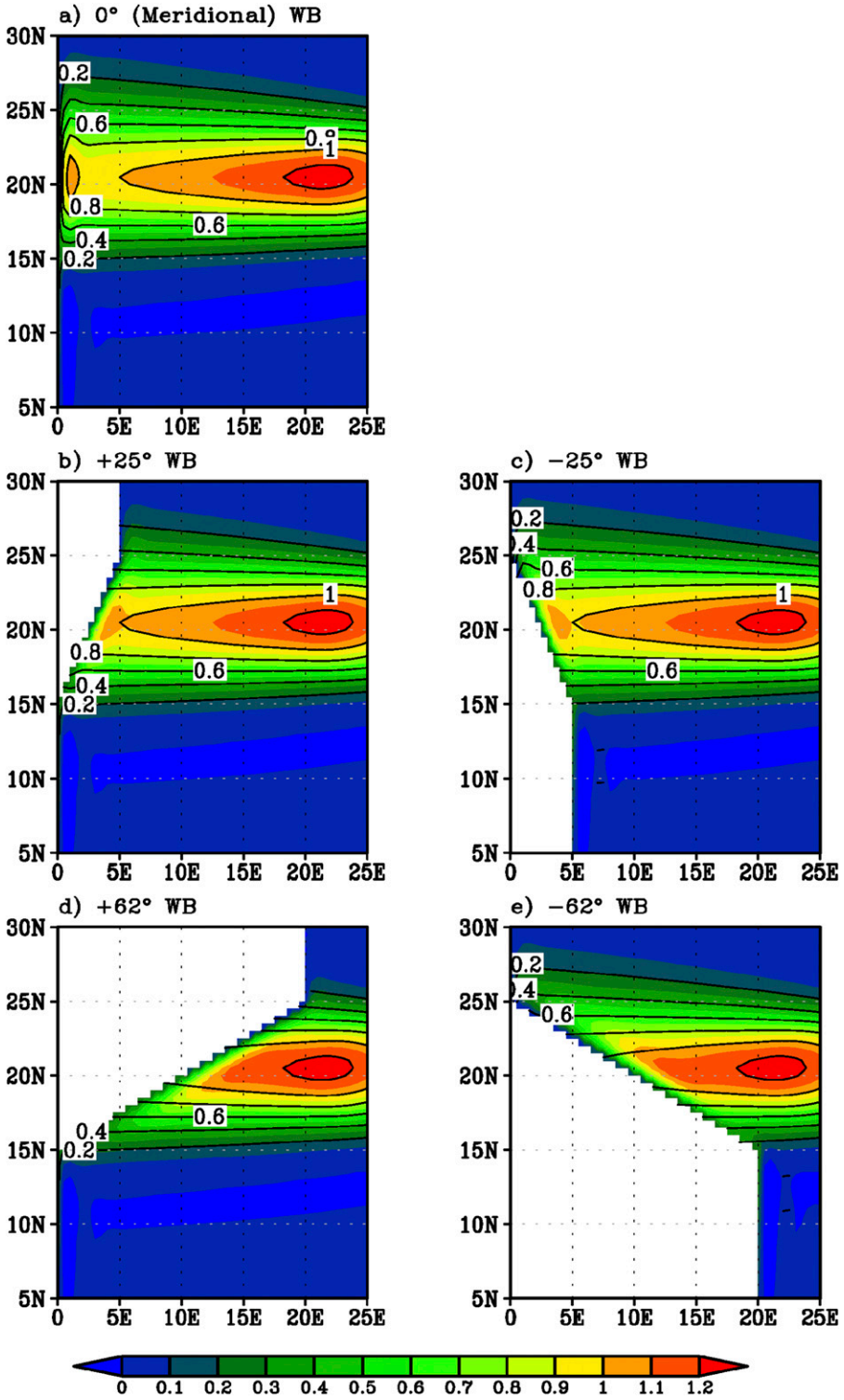

FIG. 6. Modeled sea level (color shading) for (a) meridional (0°) boundary and slanted boundaries, whose angles clockwise from due north are (b) +25° (c) −25°, (d) +62°, and (e) −62°, for steady forcing experiments. The mass-input forcing is centered at 20°N and 30°E. The contours in all panels indicate the sea level with the meridional western boundary in (a), and the sea levels are normalized by the maximal sea level along 5°E in (a) (5.6 cm).

TABLE 2. As in Table 1, but for steady forcing experiments with slanted western boundaries. The angle between the western boundary and a meridian is clockwise from due north.

Angle of western boundary	+25°	−25°	+62°	−62°
RRMSE (%)	2.9	1.9	6.7	5.2

dynamics of Eqs. (1)–(3), the sea level itself also satisfies Eq. (14). This means one can use the essence of Eq. (14) for interpretation of sea level differences shown in Fig. 1 or similar figures in previous studies (e.g., Church et al. 2013; Yin et al. 2010; Slangen et al. 2014) without knowing vertical mode contributions. To accomplish this, it is useful to provide a scaling law derived from this equation.

To derive such a scaling law, we assume that the interior sea level anomalies have a constant amplitude. In this case, Eq. (14) reduces to

$$h[x_W(y),y,t]=\frac{f(y)}{f(y_P)}h[x_W(y_P),y_P,t]+f(y)\left[\frac{1}{f(y)}-\frac{1}{f(y_P)}\right]h(x_I,y,t). \quad (20)$$

The second term can be approximated by a Taylor expansion. This leads to a scaling law or a rule of thumb for the magnitude of sea level anomalies as

$$\hat{h}_W(y)\sim\frac{f(y)}{f(y_P)}\hat{h}_W(y_P)+\frac{\beta(y_C)}{f(y_C)}L\hat{h}_I, \quad (21)$$

where $\hat{h}_W$ and $\hat{h}_I$ are the magnitudes of the WBSL and interior sea level, respectively; L is the meridional distance between northern and southern points; and y_C is the meridional position at the center of the Taylor expansion.

The rule of thumb, Eq. (21), has two important implications. First, the influence of the interior sea level is not proportional to its magnitude $\hat{h}_I$, but to the meridionally integrated mass anomalies $L\hat{h}_I$. This is important when interpreting numerical model output. Typical ocean component grid spacing of the current generation used in CMIP5 climate models is about 1°. In such low-resolution models, the narrow structures of the western boundary current and its extension are not resolved and anomalies tend to have much wider spatial extents than found in reality. However, if the meridionally integrated mass anomalies are properly simulated (e.g., Taguchi et al. 2007), this will lead to a correct WBSL magnitude in the model. In this case, if downscaling is conducted using a regional ocean model with a finer resolution, it will give a similar magnitude of WBSL to that in the climate model.

This is actually reported in a recent regional downscaling study by Liu et al. (2016), who found that the difference of future regional sea level change between the downscaled results and climate models are within 10 cm along the coast of Japan's main island of Honshu, in contrast to a much larger interior sea level difference of 20–30 cm. This suggests that downscaling may be

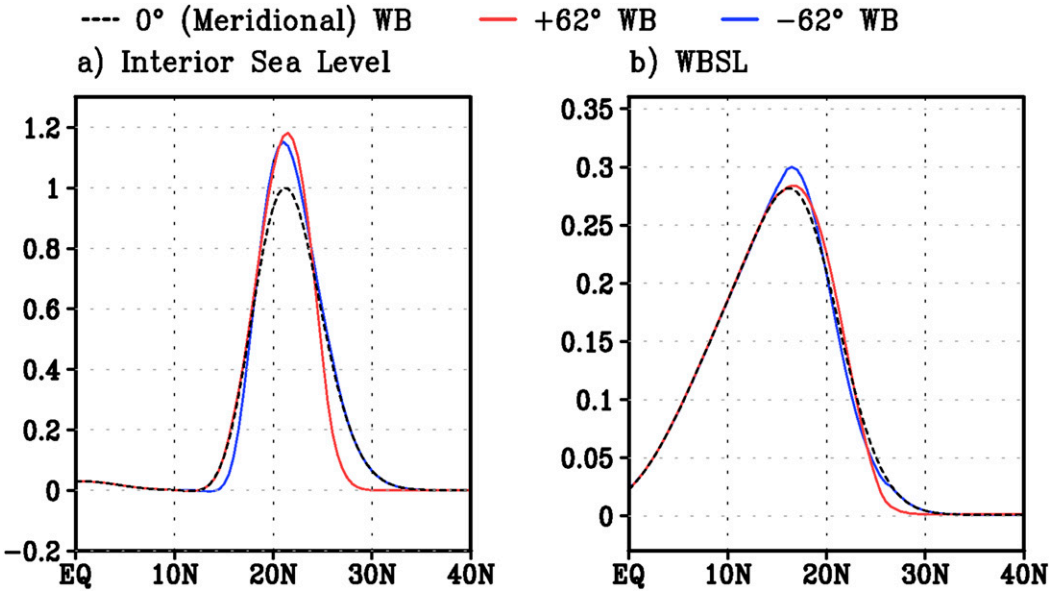

FIG. 7. (a) Sea level along the western end of ocean interior and (b) WBSL for the meridional western boundary (dashed black curve), for the slanted western boundary at a +62° angle clockwise from due north (red), and for that at a −62° angle (blue) in steady forcing experiments. The mass-input forcing is centered at 20°N and 30°E. The sea levels are normalized by the maximal sea level along 5°E in the meridional boundary experiment (5.6 cm).

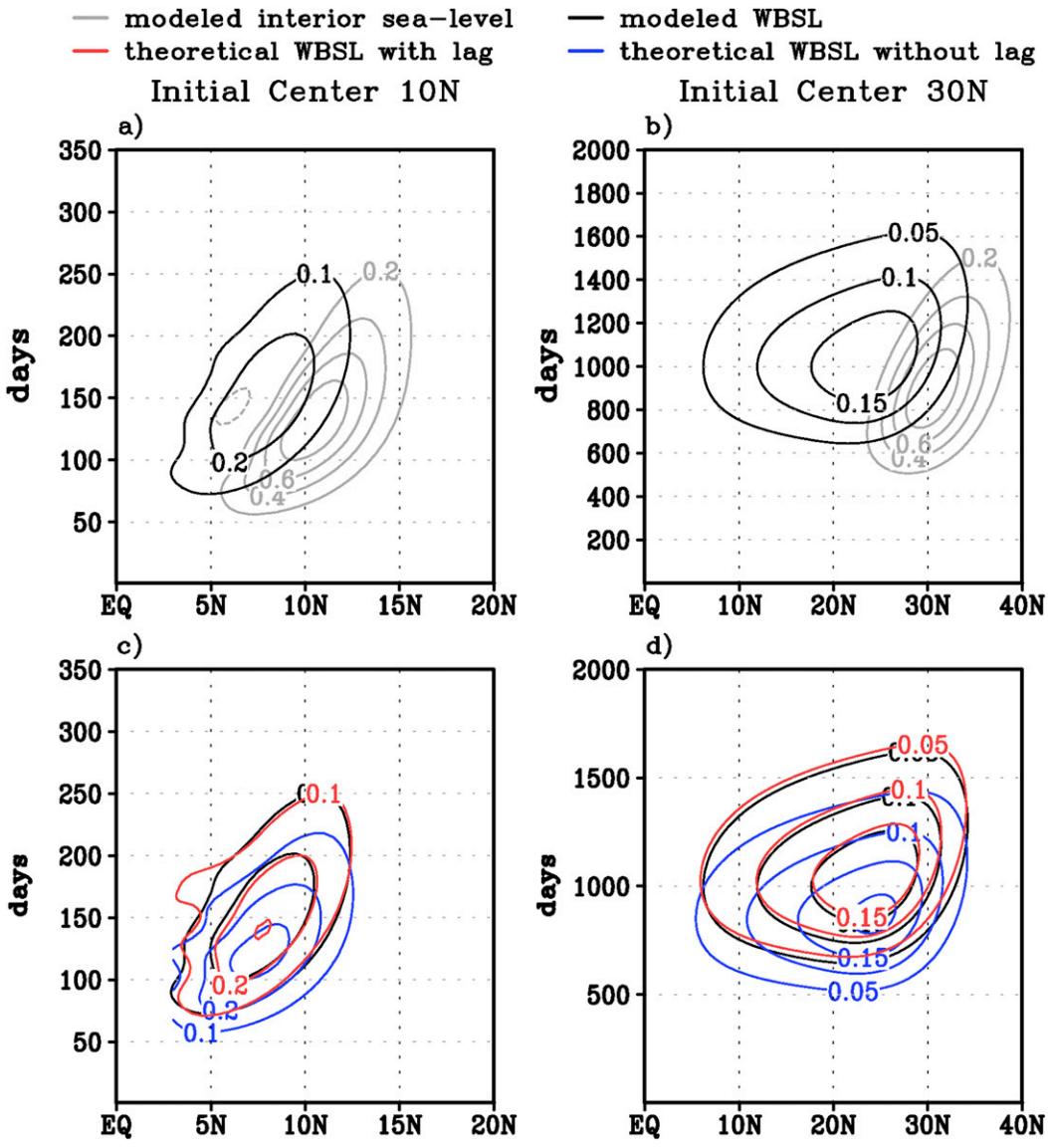

FIG. 8. Modeled sea level at the western end of ocean interior (5°E; gray contour in top panels), the modeled WBSL (black contour in top and bottom panels), the theoretical WBSL with time lag (red contours in bottom panels), and that without lag (blue contours in bottom panels) for initial sea level anomalies centered at (a),(c) 10°N and 30°E and (b),(d) 30°N and 30°E with the meridional western boundary. The sea levels are normalized by the maximal sea level along the western end of ocean interior in each experiment [65 cm for (a) and (c) and 46 cm for (b) and (d)]. The contour intervals are 0.2 for interior sea level and 0.1 (0.05) for the WBSL in the left (right) panels without zero contours.

more useful for obtaining the correct spatial distribution of WBSL than evaluating its magnitude. Such downscaling, however, can detect much larger differences at small islands separated from the western boundary, such as those found for the south Japan island of Okinawa by Liu et al. (2016).

Second, the influence of the interior sea level (northern WBSL) on the southern WBSL increases in lower (higher) latitudes. This is clearly seen in Fig. 9, which shows the factors of the interior sea level and the WBSL at the northern latitude to the southern WBSL, that is, $f(y)/f(y_P)$ and $f(y)/[1/f(y) - 1/f(y_P)]$ in Eq. (20), for latitudinal extents of 5°, 10°, and 20°. This feature can be important in interpreting the regional sea level rise. Figure 1 shows that a relatively large sea level rise will occur in midlatitudes, where the factor for the ocean interior is smaller than the factor of the high-latitude WBSL by several times (Fig. 9). This indicates that if the

TABLE 3. As in Table 1, but for initial value experiments for which the theoretical estimation is given by Eq. (19). The time delay of Rossby wave propagation is included for the upper row, but is ignored in the lower row.

Latitude of initial sea level (°N)	10	20	30	40
RRMSE (%) with delay	8.8	5.6	8.7	13.9
RRMSE (%) without delay	39.1	43.3	41.1	32.1

magnitudes of the sea level change in the ocean interior and that of high latitude are the same, the former would essentially control the sea level change in the lower latitude.

6. Application of theory to CMIP5

In this section, we examine whether the present theory can reproduce major WBSL features for future sea level rise projected in CMIP5. We use the 34 CMIP5 models summarized in Table 4 and analyze the first ensemble of each model. The number of models is about 1.5 times larger than the 21 models used in previous studies (Church et al. 2013; Slangen et al. 2014; Carson et al. 2016), and sea level changes are computed between the 2081–2100 and 1981–2000 periods under representative concentration pathway (RCP) 8.5 and historical scenarios, respectively. Note that even though RCP 8.5 is the highest emission scenario of CMIP5, the recent observed CO_2 emission level is slightly larger than that determined for this scenario (Peters et al. 2013). Sea level data are regridded onto a common $1° \times 1°$ grid by using the bilinear interpolation. For near-coast grid points where the bilinear interpolation cannot be used, the neighborhood interpolation is employed as in the Intergovernmental Panel on Climate Change Fifth Assessment Report (IPCC AR5; Church et al. 2013).

Since we are interested in the spatial patterns of sea level rise, we analyze sea level deviation from the global mean, which is referred to as dynamic sea level (DSL) in previous studies (e.g., Yin et al. 2010; Zhang et al. 2014). It is noteworthy that physical processes not included in CMIP5 models (such as land-ice melting, terrestrial water storage, and glacial isostatic adjustment) contribute to spatial patterns of sea level rise (e.g., Slangen et al. 2014). However, since they do not cause dynamical responses such as Rossby waves in the ocean, they are not included in the present analysis.

We will now examine our theory for western-boundary DSL (WBDSL) change in the North and South Atlantic Oceans. The sea level rise in the northwestern North

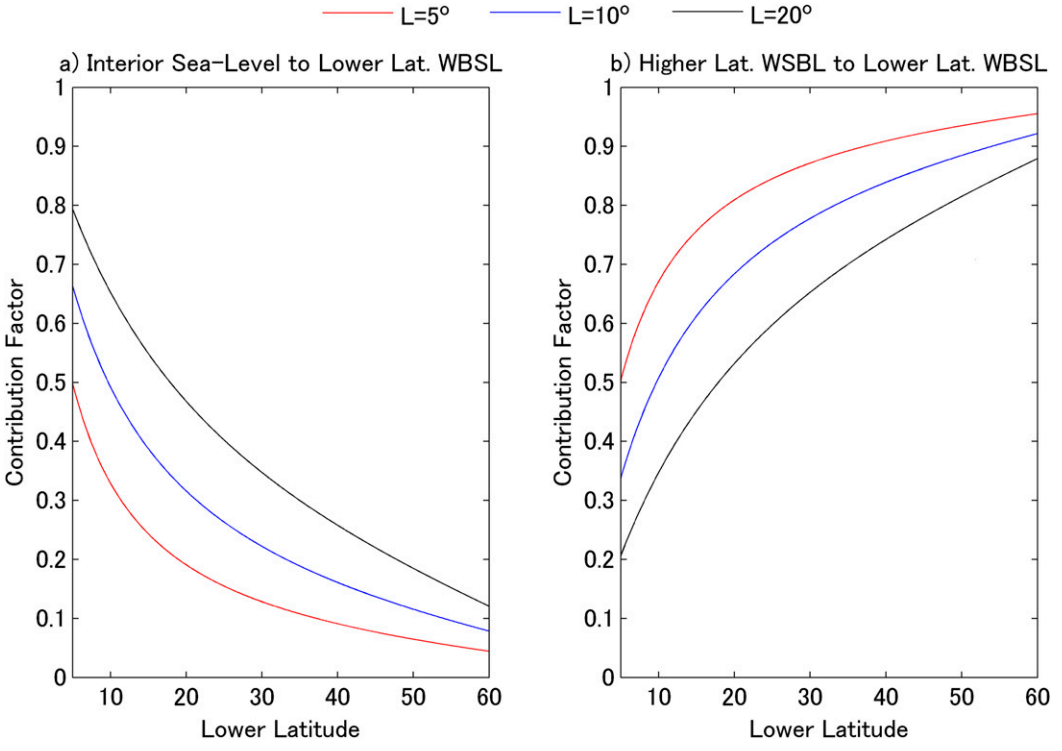

FIG. 9. Contribution factors (unitless) of (a) interior sea level to the southern WBSL and (b) higher-latitude WBSL to the lower-latitude WBSL on the right-hand side of Eq. (20) (see text) for the distance between the two latitudes of 5° (red), 10° (blue), and 20° (black). The interior sea level is assumed to be uniform across the meridional extent.

TABLE 4. Model names, institutions, number of gird points, and vertical levels of the CMIP5 models used in the present analysis.

Model	Institution	Lon grid points × lat grid points × levels
ACCESS1.0	Commonwealth Scientific and Industrial Research Organisation (CSIRO)	360 × 300 × 50
ACCESS1.3	and Bureau of Meteorology, Australia	
BCC_CSM1.1	Beijing Climate Center, China Meteorological Administration, China	360 × 232 × 40
BCC-CSM1.1-M		
CCSM4	National Center for Atmospheric Research (NCAR), United States	320 × 384 × 60
CESM1(BGC)		
CESM1(WACCM)		
CMCC-CESM	Centro Euro-Mediterraneo sui Cambiamenti Climatici, Italy	182 × 149 × 31
CMCC-CM		
CMCC-CMS		
CNRM-CM5	Centre National de Recherches Météorologiques, France	362 × 292 × 42
CSIRO Mk3.6.0	CSIRO and Queensland Climate Change Centre of Excellence, Australia	192 × 189 × 31
CanESM2	Canadian Centre for Climate Modeling and Analysis, Canada	256 × 192 × 40
FIO-ESM	First Institute of Oceanography, State Oceanic Administration, China	320 × 384 × 40
GFDL CM3	NOAA/Geophysical Fluid Dynamics Laboratory, United States	360 × 200 × 50
GFDL-ESM2G		360 × 210 × 50
GFDL-ESM2M		360 × 200 × 50
GISS-E2-R	NASA Goddard Institute for Space Studies, United States	288 × 180 × 32
GISS-E2-R-CC		
HadGEM2-CC	Met Office Hadley Centre, United Kingdom	360 × 216 × 40
HadGEM2-ES		
INM-CM4.0	Institute for Numerical Mathematics, Russia	360 × 340 × 40
IPSL-CM5A-LR	L'Institut Pierre-Simon Laplace, France	182 × 149 × 31
IPSL-CM5A-MR		
IPSL-CM5B-LR		
MIROC-ESM	Japan Agency for Marine-Earth Science and Technology, Atmosphere	256 × 192 × 44
MIROC-ESM-CHEM	and Ocean Research Institute, and National Institute for	256 × 192 × 44
MIROC5	Environmental Studies, Japan	256 × 224 × 50
MPI-ESM-LR	Max Planck Institute for Meteorology, Germany	256 × 220 × 40
MPI-ESM-MR		802 × 404 × 40
MRI-CGCM3	Meteorological Research Institute, Japan	360 × 368 × 51
MRI-ESM1		
NorESM1-M	Norwegian Climate Centre, Norway	320 × 384 × 70
NorESM1-ME		

Atlantic has recently attracted significant amounts of attention (e.g., Yin et al. 2009, 2010), and it has exhibited high sea level rise continuously from the ocean interior to the western boundary (Fig. 1). On the other hand, a high interior sea level rise prominent in the southwestern South Atlantic does not reach the coast. In addition, since WBDSL change spatial variations in these two basins are larger than those in the other basins (not shown), it would be interesting to determine whether the theory could successfully reproduce those spatial changes. Since the model coastal topographies are different from one model to another, the WBSL is found as DSL by making a selection on a 1° × 1° grid attached to the land grid to the west at each latitude.

The WBSL is defined between the Ungava peninsula and the Florida peninsula between 59° and 29°N for the North Atlantic and north of 50°S for the South Atlantic. In the present estimation, WBSL changes at the highest latitude along the western boundary and the ocean interior sea level are obtained from CMIP5 data, while WBDSL changes in the lower latitudes are estimated using Eq. (14). The width between the western boundary and the western end of the ocean interior is set to 10° in longitude, which is twice the width used in the previous section, in order to avoid the shallow shelf existing in the ocean interior. This is a crude treatment of the shallow shelf, and the presence of the shelf in reality is one of the caveats of the present theory, as will be discussed in the next section.

Figure 10 compares the theoretical estimation and CMIP5 outputs with respect to multimodel ensemble mean (MME) WBDSL change. In the North Atlantic, the theory qualitatively captures the major feature of the spatial pattern of WBDSL change in the CMIP5 MME. The WBDSL is roughly uniform from the Labrador Sea to around New York City (NYC; represented by the grid centered at 40.5°N) and declines in magnitude as it extends southward (Fig. 10a). Quantitatively,

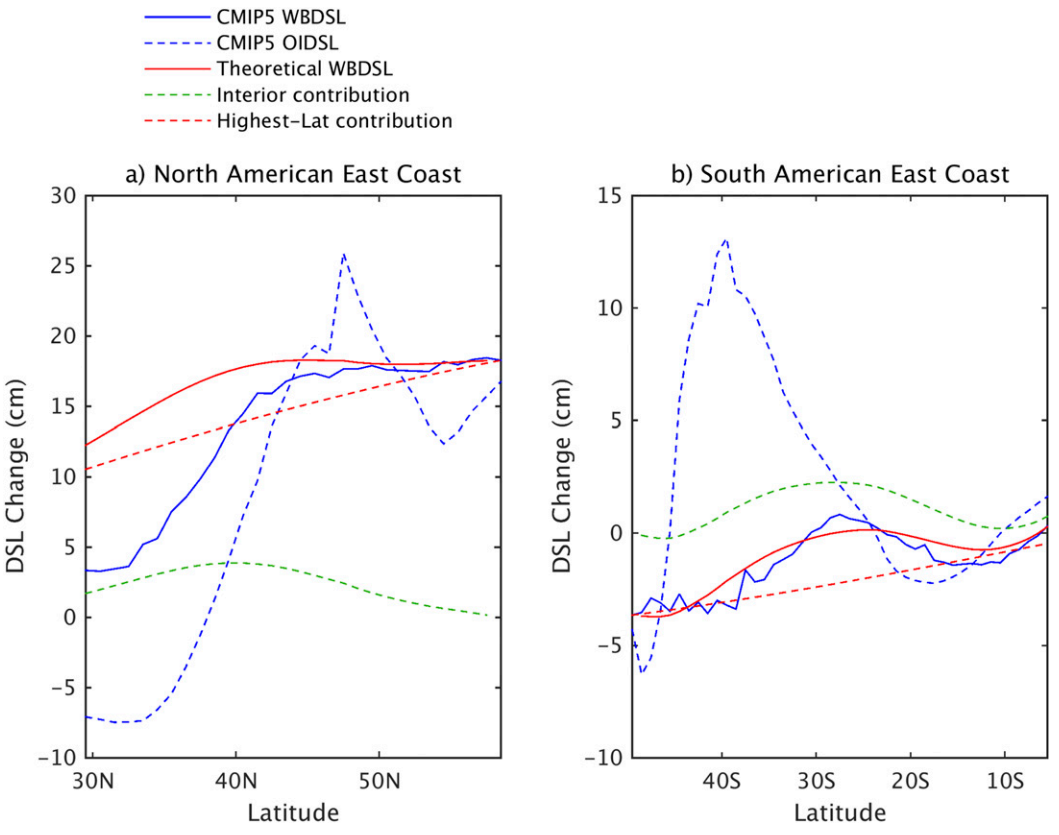

FIG. 10. DSL change estimated from the theory and obtained MME of 34 CMIP5 models between the periods of 2081–2100 and 1981–2000 under the RCP 8.5 and historical scenarios, respectively, along the western boundary in (a) the North Atlantic and (b) the South Atlantic. The DSL change in CMIP5 MME is shown for western boundary (blue solid) and along the western end of the ocean interior (blue dashed). Theoretical estimation of western boundary DSL change (red solid) is given by the sum of the contribution of the western boundary DSL change at the highest latitude in each panel (red dashed) and the contribution of the ocean interior (green dashed).

however, the theory underestimates this southward WBDSL decline. The high-latitude contribution is much larger than the ocean interior contribution (Fig. 10a), as argued in the previous section, for high-latitude WBDSLs and interior DSLs with similar magnitudes. This suggests that the sea level rise hot spot around the NYC and along the East Coast of the United States is strongly controlled by the sea level in the Labrador Sea.

In the South Atlantic, the theory reproduces reasonably well the WBSL change (Fig. 10b). More specifically, DSL changes in both the theory and CMIP5 MME increase from 50°S toward the north, reach their maximum around 25°S, and decrease farther north from 10° to 15°S. This WBDSL change meridional variability receives nearly equal contributions from the highest-latitude WBDSL and the ocean interior DSL, which is associated with the much larger ocean interior DSL change than WBDSL change. Consequently, the contribution of the ocean interior is relatively large in the South Atlantic compared to in the North Atlantic.

To know the origin of sea level rise uncertainty, that is, differences of sea level rise among CMIP5 models, the theory is applied to data obtained from each of the 34 climate models. We found that the theory well reproduces the WBDSL changes of CMIP5 models at NYC ($r = 0.93$), even though the theoretical estimate slightly overestimates the CMIP5 model results (Fig. 11a). The high-latitude contribution is larger than the ocean interior contribution in all models except for a few models that have very small amplitudes (Fig. 11b). The dominance of high-latitude WBDSL becomes stronger for total WBDSLs larger than 20 cm, thereby indicating the increasing importance of the Labrador Sea sea level for models that show large NYC sea level rises.

At southern Brazil (27.5°S), where the maximum WBDSL change is found in CMIP5 MME in Fig. 11b, the theory reproduces the WBDSL change ($r = 0.88$; Fig. 11c) reasonably well. The relative contributions of interior DSL change and high-latitude WBDSL change for southern Brazil are more variable than those for NYC (Fig. 11d).

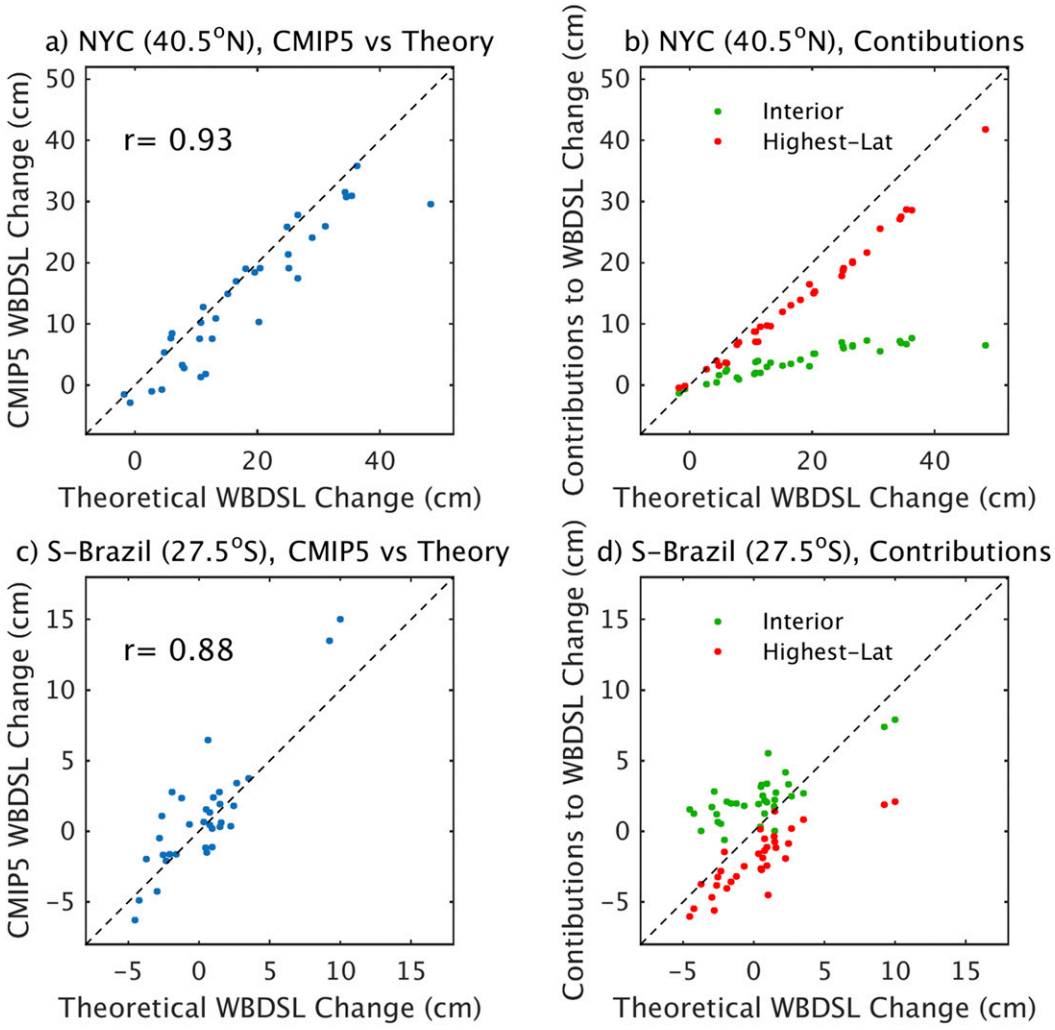

FIG. 11. WBDSL changes (a),(b) at NYC latitude (40.5°N) and (c),(d) at 27.5°S (southern Brazil) for each of the 34 CMIP5 models between the periods of 2081–2100 and 1981–2000. Panels (a) and (c) show a comparison between theoretical estimate and CMIP5 model outputs, while (b) and (d) show contributions of ocean interior DSL change and WBDSL change at the highest latitude vs the total theoretical WBDSL estimate at the aforementioned latitudes.

The strong relationship between NYC and Labrador Sea in model uncertainty is also confirmed by an independent correlation analysis. Figure 12a shows correlations between DSL changes at each grid point among the 34 models used and the NYC WBDSL changes. The strong correlations ($r > 0.9$) occur from NYC to higher latitudes up to the Labrador Sea along the western boundary. Standard deviation of DSL change among climate models has the maximum in the ocean interior, but correlations around the maximum are smaller than 0.6, indicating that the DSL change differences in the ocean interior are not strongly related to the NYC WBDSL changes. Consequently, it is strongly suggested that the Labrador Sea and NYC are connected by information propagating along the western boundary, which is consistent with the theory. For the WBDSL changes in southern Brazil, large correlations are found in the ocean interior (Fig. 12b), which is consistent with the relatively large contribution of the ocean interior DSL change for the South Atlantic that is shown in Fig. 11.

7. Discussion and conclusions

A robust relationship between the sea level along a curved western boundary and the interior sea level is derived [Eqs. (12), (14)]. Although it is derived in the reduced gravity model context, the theory is equally applicable to the barotropic one-layer model. In addition, if vertical mode superposition is appropriate within

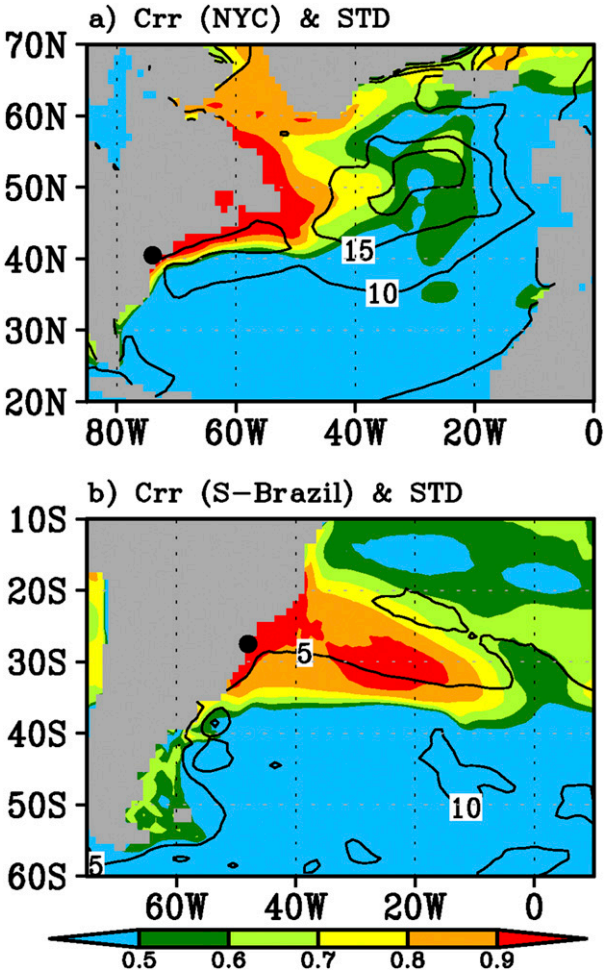

FIG. 12. Correlation coefficients between the WBDSL changes between the periods of 2081–2100 and 1981–2000 at (a) NYC and (b) southern Brazil and the DSL changes at each grid point over the 34 CMIP5 models (color shading) along with the standard deviation (contours) of the DSL changes. The contour interval is 5 cm without zero contours. Shading and contours are plotted for grid points that are in the ocean in more than 80% of models after interpolation onto a common 1° × 1° grid.

the WBL with linear dynamics working for each mode on long time scales, the theory given by Eq. (14) can be directly used to evaluate the sea level itself without knowing the contribution of each vertical mode. The theory provides good estimations of WBSL simulated in the reduced gravity model across different horizontal diffusion coefficients, model grid resolutions, and lateral boundary conditions (Figs. 3–8). Furthermore, it leads to a ''rule of thumb'' via Eq. (21). The rule of thumb indicates that the impact of the ocean interior sea level depends on the meridional integral of mass anomalies, suggesting that the magnitudes of WBSL in low- and high-resolution models will not be much different. Also, the influence of the ocean interior sea level (northern WBSL) on the southern WBSL increases in lower (higher) latitudes (Fig. 9).

We applied the theory to the DSL rise of CMIP5 models between the periods of 2081–2100 and 1981–2000 with RCP 8.5 and historical scenarios, respectively, for the east coast of North and South America. The results showed that the theory reproduces a near-uniform WBDSL rise north of 40°N and a weaker rise south of it, as is found in quantitative CMIP5 MME, even though it underestimates the southward reduction rate of the WBDSL rise (Fig. 10). The theory suggests that the Labrador Sea exerts a dominant influence on the sea level rise hot spot in northeastern North America, with much weaker sea level change contribution in the ocean interior, for both MME (Fig. 10) and model uncertainty (Fig. 11), which was confirmed by an independent correlation analysis (Fig. 12). Yin et al. (2009) suggested that the NYC sea level rise is associated with the changes of the Labrador Sea and Atlantic meridional overturning circulation (AMOC). Our results suggest that, rather than AMOC, the sea level rise in the Labrador Sea has a more direct impact on NYC sea level rise, though the deep convection of the Labrador Sea is an important part of the AMOC. The theory also successfully reproduces the spatial pattern of WBDSL change along the South American east coast, with a somewhat larger contribution for the ocean interior when compared with that in the North Atlantic (Fig. 10).

The present theory is based on a linear reduced gravity model and includes sea levels that can be expressed by the superposition of vertical modes with linear dynamics. Hence, several factors may limit application of the theory in realistic situations such as those examined in section 6. Those factors may be categorized into 1) nonlinear dynamics, 2) mechanisms that bring coupling among vertical modes, and 3) linear dynamics that cannot be captured by vertical modes. Below we discuss these factors.

First, nonlinear advection due to strong western boundary currents, such as the Gulf Stream, can be important if they modify the propagation of long Rossby waves. The non-Doppler shift effect is expected in the one-layer model context, which suggests that the Rossby wave of the first vertical mode is less affected by the mean current (Liu 1999). It is interesting to note that recent studies show that extensions of the Gulf Stream and the Kuroshio act as waveguides for jet-trapped Rossby waves (Sasaki and Schneider 2011a,b; Sasaki et al. 2013).

These jet-trapped Rossby waves, arising from the potential vorticity conservation, are trapped by zonal jets with small meridional extents and have different characteristics than long Rossby waves, which have larger spatial scales in both the zonal and meridional

directions. Nevertheless, the zonal propagation of the jet-trapped Rossby wave along the jet is essentially governed by Eq. (6). Therefore, the influence of jet-trapped Rossby waves can be explained by the present theory. Indeed, based on observational data analysis, Sasaki et al. (2014) reported that the jet-trapped Rossby wave along the Kuroshio Extension incidental to the Japan coast impacts the coastal sea level around the Kuroshio Extension latitude and southward, which is consistent with the present theory. This indicates that the theory might work for the first vertical mode with the presence of the western boundary currents. The strong mean flows, however, can substantially alter Rossby wave propagation of higher vertical modes, possibly resulting in sea levels that cannot be well captured by the theory because of those higher modes.

Second, vertical modes are no longer independent when they interact within the presence of bottom topography. In general, nonflat bottom topography causes vertical mode interactions, including barotropic and baroclinic energy conversions such as the joint effect of baroclinicity and relief (JEBAR; Mertz and Wright 1992), which is important in subarctic circulation in the North Atlantic (Yeager 2015), modal interaction over a sloping boundary (Dewar and Hogg 2010), and the influence of the deep western boundary current on the surface flow including the Gulf Stream (Zhang and Vallis 2007). If these mechanisms cause vertical mode interactions within the WBL, they cannot be represented by the present theory.

In addition, to a larger meridional extent, the background stratification can change substantially, thereby resulting in changes in vertical mode structures, and thus interactions among the modes along the equatorward propagation could occur. It is noteworthy that Yin and Goddard (2013) suggested that the baroclinic (barotropic) processes will play important roles to the north (south) of Cape Hatteras in future sea level rises in the northeast coast of North America. This could be a reason why the theory underestimates the southward decrease of the sea level rise found in section 6, even though the dynamical processes that cause such vertical mode structures are not clear.

Third, mechanisms that are not included in the context of vertical mode decomposition can also play important roles. One such mechanism may be gravity wave propagation over shallow shelves. For example, Yin et al. (2010) showed that the sea levels in deep basins propagate into shallow shelves associated with gravity waves. This suggests that the sea levels over such shelves are primarily controlled by the sea level over the deep ocean and that the presence of a shelf probably modifies the sea level from that without the shelf to some extent. In future studies, it will be important to identify the strength of such modifications.

These possible caveats indicate that there are many improvements to be made in further studies. The simplicity of the present theory, we believe, serves as a good starting point for further improvements. Such improvements may result from further theoretical studies and numerical experiments using both simple models and realistic OGCMs. By achieving a better understanding and more accurate predictions and projections of sea level variability and changes along the western boundary, these future studies will help society to better prepare for possible problems arising from sea level variability and change.

Acknowledgments. S.M. is supported by the Japan Society for the Promotion of Science (JSPS) KAKENHI Grants 26287110, 26610146, and 15H01606, and by the Joint Institute for Marine and Atmospheric Research at the University of Hawaii. B.Q. is supported by the U.S. National Aeronautics and Space Administration (NASA) Ocean Surface Topography Science Team (OSTST) Grants NNX13AE51E and NNX17AH33G. N.S. is supported by U.S. National Science Foundation Grant OCE1357015. The authors deeply appreciate the constructive comments of Dr. Xiaoming Zhai and our anonymous reviewer.

APPENDIX

Validity of Geostrophic Approximation for Meridional Velocity

In this appendix, we show that the meridional velocity can be approximated by geostrophic velocity even for the nonmeridional western boundary unless the angle between the western boundary and a meridian, ϕ in Fig. 2, is not extremely large. The meridional velocity can be written as

$$v = u_l \cos\phi + u_n \sin\phi, \tag{A1}$$

where u_n and u_l are, respectively, the perpendicular and parallel components of the velocity with respect to the western boundary, and ϕ is the angle between the western boundary and a meridian. We assume that the perpendicular velocity is dominated by its ageostrophic component u_n^a, while the parallel velocity has geostrophic and ageostrophic components u_l^g and u_l^a, and $|u_l^g| \gg |u_l^a|$ and $|u_l^g| \gg |u_n^a|$. Thus, the meridional velocity is given by $v = (u_l^g + u_l^a)\cos\phi + u_n^a \sin\phi$. The condition that the meridional velocity is dominated by the geostrophic component is, therefore,

$$\left|\frac{u_l^g}{u_n^a}\right| \gg \tan\phi. \tag{A2}$$

Note that $\tan\phi$ is of order one or less for small or moderate angles, because even for an angle of 60°,

$\tan\phi$ is just 1.7. Consequently, unless the western boundary is very steeply slanted from a meridian, it can be assumed that the meridional velocity is well approximated by the geostrophic velocity.

REFERENCES

Bryan, K., 1969: A numerical model for the study of the circulation of the world ocean. *J. Comput. Phys.*, **4**, 347–376, doi:10.1016/0021-9991(69)90004-7.

Carson, M., A. Köhl, D. Stammer, A. B. A. Slangen, C. A. Katsman, R. S. W. van de Wal, J. Church, and N. White, 2016: Coastal sea level changes, observed and projected during the 20th and 21st century. *Climatic Change*, **134**, 269–281, doi:10.1007/s10584-015-1520-1.

Cessi, P., and S. Louazel, 2001: Decadal oceanic response to stochastic wind forcing. *J. Phys. Oceanogr.*, **31**, 3020–3029, doi:10.1175/1520-0485(2001)031<3020:DORTSW>2.0.CO;2.

Church, J. A., and Coauthors, 2013: Sea level change. *Climate Change 2013: The Physical Science Basis*, T. F. Stocker et al., Eds., Cambridge University Press, 1137–1216.

Dewar, W. K., and A. M. Hogg, 2010: Topographic inviscid dissipation of balanced flow. *Ocean Modell.*, **32**, 1–13, doi:10.1016/j.ocemod.2009.03.007.

Di Lorenzo, E., and Coauthors, 2008: North Pacific gyre oscillation links ocean climate and ecosystem change. *Geophys. Res. Lett.*, **35**, L08607, doi:10.1029/2007GL032838.

Durand, F., D. Shankar, F. Birol, and S. S. C. Shenoi, 2009: Spatiotemporal structure of the East India Coastal Current from satellite altimetry. *J. Geophys. Res.*, **114**, C02013, doi:10.1029/2008JC004807.

Godfrey, J. S., 1975: On ocean spindown. I: A linear experiment. *J. Phys. Oceanogr.*, **5**, 399–409, doi:10.1175/1520-0485(1975)005<0399:OOSIAL>2.0.CO;2.

Johnson, H. L., and D. P. Marshall, 2002: A theory for the surface Atlantic response to thermohaline variability. *J. Phys. Oceanogr.*, **32**, 1121–1132, doi:10.1175/1520-0485(2002)032<1121:ATFTSA>2.0.CO;2.

Kessler, W. S., and L. Gourdeau, 2007: The annual cycle of circulation of the southwest subtropical Pacific analyzed in an ocean GCM. *J. Phys. Oceanogr.*, **37**, 1610–1627, doi:10.1175/JPO3046.1.

Liu, Z., 1999: Planetary waves in the thermocline: Non-Doppler shift mode, advective mode and Green mode. *Quart. J. Roy. Meteor. Soc.*, **125**, 1315–1339, doi:10.1002/qj.1999.49712555611.

——, L. Wu, and E. Bayler, 1999: Rossby wave–coastal Kelvin wave interaction in the extratropics. Part I: Low-frequency adjustment in a closed basin. *J. Phys. Oceanogr.*, **29**, 2382–2404, doi:10.1175/1520-0485(1999)029<2382:RWCKWI>2.0.CO;2.

Liu, Z.-J., S. Minobe, Y. N. Sasaki, and M. Terada, 2016: Dynamical downscaling of future sea-level change in the western North Pacific using ROMS. *J. Oceanogr.*, **72**, 905–922, doi:10.1007/s10872-016-0390-0.

Marshall, D. P., and H. L. Johnson, 2013: Propagation of meridional circulation anomalies along western and eastern boundaries. *J. Phys. Oceanogr.*, **43**, 2699–2716, doi:10.1175/JPO-D-13-0134.1.

Mertz, G., and D. G. Wright, 1992: Interpretations of the JEBAR Term. *J. Phys. Oceanogr.*, **22**, 301–305, doi:10.1175/1520-0485(1992)022<0301:IOTJT>2.0.CO;2.

Milliff, R. F., and J. C. McWilliams, 1994: The evolution of boundary pressure in ocean basins. *J. Phys. Oceanogr.*, **24**, 1317–1338, doi:10.1175/1520-0485(1994)024<1317:TEOBPI>2.0.CO;2.

Nicholls, R. J., and A. Cazenave, 2010: Sea-level rise and its impact on coastal zones. *Science*, **328**, 1517–1520, doi:10.1126/science.1185782.

Pedlosky, J., 1996: *Ocean Circulation Theory*. Springer, 453 pp.

Peters, G. P., and Coauthors, 2013: The challenge to keep global warming below 2°C. *Nat. Climate Change*, **3**, 4–6, doi:10.1038/nclimate1783.

Qiu, B., and S. Chen, 2012: Multidecadal sea level and gyre circulation variability in the northwestern tropical Pacific Ocean. *J. Phys. Oceanogr.*, **42**, 193–206, doi:10.1175/JPO-D-11-061.1.

Sasaki, Y. N., and N. Schneider, 2011a: Decadal shifts of the Kuroshio Extension jet: Application of thin-jet theory. *J. Phys. Oceanogr.*, **41**, 979–993, doi:10.1175/2010JPO4550.1.

——, and ——, 2011b: Interannual to decadal Gulf Stream variability in an eddy-resolving ocean model. *Ocean Modell.*, **39**, 209–219, doi:10.1016/j.ocemod.2011.04.004.

——, S. Minobe, N. Schneider, T. Kagimoto, M. Nonaka, and H. Sasaki, 2008: Decadal sea level variability in the South Pacific in a global eddy-resolving ocean model hindcast. *J. Phys. Oceanogr.*, **38**, 1731–1747, doi:10.1175/2007JPO3915.1.

——, ——, and ——, 2013: Decadal response of the Kuroshio extension jet to Rossby waves: Observation and thin-jet theory. *J. Phys. Oceanogr.*, **43**, 442–456, doi:10.1175/JPO-D-12-096.1.

——, ——, and Y. Miura, 2014: Decadal sea-level variability along the coast of Japan in response to ocean circulation changes. *J. Geophys. Res. Oceans*, **119**, 266–275, doi:10.1002/2013JC009327.

Schopf, P. S., D. L. T. Anderson, and R. Smith, 1981: Beta-dispersion of low-frequency Rossby waves. *Dyn. Atmos. Oceans*, **5**, 187–214, doi:10.1016/0377-0265(81)90011-7.

Slangen, A. B. A., M. Carson, C. A. Katsman, R. S. W. van de Wal, A. Köhl, L. L. A. Vermeersen, and D. Stammer, 2014: Projecting twenty-first century regional sea-level changes. *Climatic Change*, **124**, 317–332, doi:10.1007/s10584-014-1080-9.

Sueyoshi, M., and T. Yasuda, 2012: Inter-model variability of projected sea level changes in the western North Pacific in CMIP3 coupled climate models. *J. Oceanogr.*, **68**, 533–543, doi:10.1007/s10872-012-0117-9.

Suzuki, T., and M. Ishii, 2011a: Regional distribution of sea level changes resulting from enhanced greenhouse warming in the Model for Interdisciplinary Research on Climate version 3.2. *Geophys. Res. Lett.*, **38**, L02601, doi:10.1029/2010GL045693.

——, and ——, 2011b: Long-term regional sea level changes due to variations in water mass density during the period 1981–2007. *Geophys. Res. Lett.*, **38**, L21604, doi:10.1029/2011GL049326.

Taguchi, B., S. P. Xie, N. Schneider, M. Nonaka, H. Sasaki, and Y. Sasai, 2007: Decadal variability of the Kuroshio Extension: Observations and an eddy-resolving model hindcast. *J. Climate*, **20**, 2357–2377, doi:10.1175/JCLI4142.1.

Tsujino, H., H. H. Nakano, and T. Motoi, 2008: Mechanism of currents through the straits of the Japan Sea: Mean state and seasonal variation. *J. Oceanogr.*, **64**, 141–161, doi:10.1007/s10872-008-0011-7.

Vallis, G. K., 2006: Atmospheric and oceanic fluid dynamics: Fundamentals and large-scale circulation. Cambridge University Press, 745 pp.

Yeager, S., 2015: Topographic coupling of the Atlantic overturning and gyre circulations. *J. Phys. Oceanogr.*, **45**, 1258–1284, doi:10.1175/JPO-D-14-0100.1.

Yin, J. J., 2012: Century to multi-century sea level rise projections from CMIP5 models. *Geophys. Res. Lett.*, **39**, L17709, doi:10.1029/2012GL052947.

——, and P. B. Goddard, 2013: Oceanic control of sea level rise patterns along the East Coast of the United States. *Geophys. Res. Lett.*, **40**, 5514–5520, doi:10.1002/2013GL057992.

——, M. E. Schlesinger, and R. J. Stouffer, 2009: Model projections of rapid sea-level rise on the northeast coast of the United States. *Nat. Geosci.*, **2**, 262–266, doi:10.1038/ngeo462.

——, S. M. Griffies, and R. J. Stouffer, 2010: Spatial variability of sea level rise in twenty-first century projections. *J. Climate*, **23**, 4585–4607, doi:10.1175/2010JCLI3533.1.

Zhai, X., H. L. Johnson, and D. P. Marshall, 2014: A simple model of the response of the Atlantic to the North Atlantic Oscillations. *J. Climate*, **27**, 4052–4069, doi:10.1175/JCLI-D-13-00330.1.

Zhang, R., and G. K. Vallis, 2007: The role of bottom vortex stretching on the path of the North Atlantic Western Boundary Current and on the Northern Recirculation Gyre. *J. Phys. Oceanogr.*, **37**, 2053–2080, doi:10.1175/JPO3102.1.

Zhang, X. B., J. A. Church, S. M. Platten, and D. Monselesan, 2014: Projection of subtropical gyre circulation and associated sea level changes in the Pacific based on CMIP3 climate models. *Climate Dyn.*, **43**, 131–144, doi:10.1007/s00382-013-1902-x.